SPP1^{+} macrophages promote the growth and metastasis of intrahepatic cholangiocarcinoma via OSM and THBS1 signaling

Tingjie Wang[1,3*], Ruitao Long[2*], Zhongyu Cheng[2], Mi Zhang[2], Bing Wei[1,3], Cong Lyu[1,3], Xinyue, Zhang[1,3], Cuiyun Zhang[1,3], Guangbo Tang[4], Zihang Li[5], Lei Li[2], Yida Li[6], Xiaofei Zhu[7], Chao Shi[1,3], Ke Yang[1,3], Chuanrui Xu[2#]

*Tingjie Wang and Ruitao Long contributed equally to this work.

[1]Department of Molecular Pathology, The Affiliated Cancer Hospital of Zhengzhou University, Henan Cancer Hospital, Zhengzhou, Henan, People's Republic of China.

[2]School of Pharmacy, Tongji Medical College, Huazhong University of Science and Technology, Wuhan, Hubei, China

[3]Henan Key Laboratory of Molecular Pathology, Zhengzhou, Henan, People's Republic of China.

[4]Department of Clinical Medicine Research Center, The First Affiliated Hospital of Gannan Medical University, Ganzhou, Jiangxi, People's Republic of China.

[5]Department of Hematology, The First Affiliated Hospital of Xi'an Jiaotong University, No.277 Yanta West Road, Xi'an, Shaanxi, People's Republic of China.

[6]Department of Chemistry & Loker Hydrocarbon Research Institute, University of Southern California, Los Angeles, California, United States.

[7]Henan Key Laboratory of Immunology and Targeted Drugs, Xinxiang Key Laboratory of Tumor Microenvironment and Immunotherapy, School of Medical Technology, Xinxiang Medical University, Xinxiang, Henan, People's Republic of China.

Correspondence:

Address correspondence to: Chuanrui Xu, School of Pharmacy, Tongji Medical College, Huazhong University of Science and Technology, Wuhan, Hubei, China. Email: xcr@hust.edu.cn

Conflict of interest:

The authors declare no conflicts of interest to this work.

Abbreviations

TAMs, tumor-associated macrophages; ICC, intrahepatic cholangiocarcinoma; TME, tumor microenvironment; EMT, epithelial mesenchymal transition; BMDMs, bone marrow-derived macrophages. scRNA-seq, single cell RNA sequencing; spRNAseq, spatial transcriptomics sequencing.

Funding:

The research was supported by grants from the National Natural Science Foundation of China (82472988, 82403200, 82372667, 82273059 and 82573814), Henan Province and Ministry of Health of Medical Science and Technology Program (SBGJ202302028 for T.W. and SBGJ202402032 for C.L.), and Henan Province Clinical Research-Oriented Physician Training Program (HNCRD202413).

Authors contributions:

C.X., T.W. designed the study. T.W., X.Z., and C.Z. analyzed the multi-omics data. R.L. performed experiments. T.W., R.L. wrote the manuscript. C.X. revised the article. Z.C., M.Z., C.L., B.W., L.L., X.Z. handled sample preparation. Y.L., G.T., C.S., K.Y., Z.L. managed data collection, organization. All authors read and approved the manuscript.

Data availability:

The scRNA-seq data generated in this study are available from the GEO database under accession code GSE308574. The remaining data are available within the

manuscript, supplementary information, or from the corresponding author upon reasonable request.

Abstract

Background & Aims: Tumor-associated macrophages (TAMs) are abundant in intrahepatic cholangiocarcinoma (ICC), correlate with poor prognosis, but their spatiotemporal behavior and non-immune-suppressive roles in ICC progression remain unclear. This study sought to define transcriptional heterogeneity of TAMs and map their interactions with ICC cells that promote malignancy beyond immune suppression.

Methods: We employed three mouse ICC models, four clinical ICC patient datasets, and three spatial transcriptomic platforms to chart the macrophage landscape over time and space. Cell-cell communication analysis plus phosphoproteomics guided functional validation via TAM-ICC co-culture, cytokine treatment, gene silencing/knockout, orthotopic and metastatic ICC models, and three conditional knockout mice. A prognostic ICC tissue microarray with multiplex immunofluorescence and combinatorial blockade in mice tested the efficacy of dual target inhibition.

Results: In advanced ICC tissues, an M2-like subset Mφ_SPP1, defined by high expression of *SPP1*, *VEGFA*, *ARG1,* and *GPNMB*, emerged as the major macrophage population, correlating with poor prognosis and spatially localizing to the tumor boundary. Further, Mφ_SPP1 drove ICC cell proliferation via the OSM-OSMR-STAT3-CCND1 and promoted invasion through THBS1-CD47-mTOR-DBN1 signalling. OSM and THBS1 were co-elevated in ICC patient samples; dual blockade of both targets in mouse models resulted in superior

inhibition of ICC progression.

Conclusions: Mφ_SPP1 TAMs accumulate at the tumor boundary in late-stage ICC, driving proliferation and invasion via *OSM* and *THBS1* signalling, underscoring the potential of macrophage-targeted therapy in ICC.

Keywords: Intrahepatic cholangiocarcinoma, Spatiotemporal omics, $SPP1^{+}$Macrophage, OSM, THBS1

Introduction

Intrahepatic cholangiocarcinoma (ICC), originating from the intrahepatic bile duct epithelium, shows a rising global incidence. Its subtle early symptoms, aggressive nature, and chemotherapy resistance contribute to a 5-year survival rate of below 10%.[1]

Targeted therapies and immune checkpoint inhibitors provide benefits in some solid tumors, but responses in ICC remain inconsistent owing to its complex tumor microenvironment (TME).[2] Tumor-associated macrophages (TAMs), the most abundant immune cells in the ICC TME, promote immune suppression, angiogenesis, and stromal remodelling,[2, 3] fueling progression and metastasis. Current TAM-targeting strategies—depletion, reprogramming, recruitment control, and functional regulation—show variable efficacy.[4, 5] Thus, dissecting communication cascades between ICC cells and TAMs is critical to identify therapeutic targets that directly modulate ICC.

Distinct TAM phenotypes are associated with ICC progression. MARCO^{+} TAMs correlate with epithelial mesenchymal transition (EMT), angiogenesis, and hypoxia.[6] *S100P* and *SPP1*-markers distinguishing perihilar and peripheral cholangiocarcinoma, show differential macrophage infiltration tied to prognosis and grade.[7]

Spatial distribution further influences TAM functions.[8] Spatial-omics have highlighted TAM heterogeneity.[9, 10] TAMs at invasive fronts mainly express pro-angiogenic factors such as VEGFA, while core TAMs activate immunosuppressive pathways.[6] Moreover, TAM plasticity is shaped by cues such as extracellular matrix (ECM) gradients, lactate accumulation, and cytokines.[9] However, the spatial dynamics and underlying mechanisms of TAM to promote ICC

development remain poorly defined.

Here, we integrated temporal-spatial transcriptomics to track TAMs' evolution, mapping their transcriptional and regulatory landscapes, and uncovering the human-mouse conserved TAM population driving ICC progression. Using cell-cell communication analysis, cell-cell co-culture, multiplex immunofluorescence, and knockout mouse models, we validated the critical TAM-ICC signaling axes, encompassing the key ligand-receptor pair and its downstream pathway, which promote ICC proliferation and migration. These findings are expected to elucidate direct, non-immunosuppressive pro-tumoral mechanisms in TAMs, ultimately supporting the development of macrophage-targeted immunotherapy for ICC.

Materials and methods

Animal Models

Wild-type FVB and C57BL/6 mice were purchased from Beijing Vital River Laboratory Animal Technology Co., Ltd. (Beijing, China). Genetically modified mice were provided by Shulaibao Biotechnology Co., Ltd. (Wuhan, China). All laboratory mice were kept in a specific pathogen-free environment. Experimental protocols involving animals were approved by the Ethics Committee of Huazhong University of Science and Technology. Detailed information on the animals used in this study is provided in Supplementary Table S1.

Cell source

The human cholangiocarcinoma cell lines HuCCT1, RBE, and QBC939, as well as the mouse fibroblast cell line L929 and macrophage cell line RAW 264.7, were used in this study. HuCCT1 was obtained from the Japanese Collection of Research Bioresources Cell Bank (JCRB, Osaka, Japan; accession number JCRB0425). RBE was acquired from the China Center for Type Culture Collection (Wuhan, China; accession number GDC0765). QBC939 was purchased from Shanghai Jinyuan Biological Technology Co., Ltd (Shanghai, China; product code JY-Y1457). The mouse cell lines L929 (ATCC® CCL-1™) and RAW 264.7 (ATCC® TIB-71™) were

purchased directly from the American Type Culture Collection (ATCC, Manassas, VA, USA). All cells were cultured according to the providers' recommendations and were routinely tested for mycoplasma contamination.

BR cells, isolated from BMI1/NRAS-driven primary ICC tissues in FVB mice, were maintained in RPMI-1640 complete medium supplemented with 10% fetal bovine serum and 1% penicillin-streptomycin at 37 °C with 5% CO_2 in an incubator. These cells displayed consistent in vitro growth characteristics and were capable of forming tumors in both subcutaneous and orthotopic liver implantation models in wild-type FVB mice. IHC and histopathological analysis confirmed the presence of ICC features.

Establishment of the ICC mouse model

Hydrodynamic tail vein injection was performed in 6–8 week mice to establish primary ICC mouse models. For the AKT1/NICD1 ICC mouse model, a mixture of plasmids, including 15 μg pT3-EF1aH-myr-AKT, 15 μg pT3-EF1a-NICD1, and 1.5 μg pCMV-SB, was diluted in 2 mL of sterile saline and filtered through a 0.22 μm membrane to remove impurities. For the AKT1/YAP1 ICC mouse model, a mixture of plasmids, including 15 μg pT3-EF1aH-myr-AKT, 15 μg pT3-EF1αH-YAPS127A, and 1.5 μg pCMV-SB, was diluted in 2 mL of sterile saline. For the sgP19/KRAS high-metastasis ICC model, a mixture of plasmids, including 10 μg CRISPR-Cas9-sgP19, 25 μg pT3-EF1α-KRAS, and 5.0 μg pCMV-SB, was diluted in 2 mL of sterile saline. The injection volume for a mouse weighing 20 g was 2 mL and adjusted according to body weight. Mice were restrained on a tail vein visualization platform, and the injection was completed within 5–7 s. Mice were euthanized and dissected upon reaching predefined tumor endpoint criteria.

The plasmids were generously provided by Dr. Xin Chen (University of Hawai‘i Cancer Center). Bacterial cultures were grown in Luria-Bertani medium containing 100 μg/mL ampicillin at 37°C with shaking at 180 rpm for 12 h, followed by plasmid extraction using the Omega plasmid purification kit.

165 Detailed protocols for all other *in vivo* and *in vitro* experiments, along with analytical
166 procedures, are described in the Supplementary Methods.

167 **Bioinformatic analyses**

168 scRNA-seq, spatial transcriptomics, and phosphoproteomics were performed.
169 Detailed methods are provided in the Supplementary Methods.

170

Results

Mφ_SPP1 is enriched in ICC and is associated with poor prognosis of patients with ICC

To dissect macrophage subsets driving ICC malignancy, we established an AKT1/NICD1 induced ICC mouse model via hydrodynamic tail vein injection and collected liver tissue at day 7 (early ICC), 15 (middle ICC), 25 (middle/advanced ICC), and 31 (advanced ICC). Single-cell RNA sequencing (scRNA-seq) was performed at all stages (Table S2, Fig. S1A). We identified macrophage and the other eight cell types (Fig. 1A, S1A). Then, we re-clustered macrophage cells and obtained six subtypes (Mφ_Cxcl9, Mφ_Clec4f, Mφ_Mki67, Mφ_S100a, Mφ_Dnajb1 and Mφ_Spp1, Fig. 1B). By conducting the tissue distribution via $R_{o/e}$ values and pathway enrichment analysis of macrophage subtypes, Mφ_Mki67 and Mφ_S100a were evenly distributed across all stages of ICC progression in mice and enriched with pathways related to self-proliferation and anti-tumor immune, suggesting they are not related to ICC progression (Fig. 1B, S1B-C). Mφ_Cxcl9 and Mφ_Clec4f showed dominated infiltration in the early and middle-stages of ICC progression, and were enriched for pathways related to anti-tumor immune response and pathways connected to tissue repair and maintenance of homeostasis, respectively (Fig. 1B, S1B). Therefore, they are macrophage subtypes not related to ICC progression as well. In contrast, Mφ_Dnajb1 and Mφ_Spp1 were markedly infiltrated in the middle/advanced or advanced stages and enriched with pathways promoting the proliferation of epithelial cells (Fig. 1B) Of note, Mφ_Spp1 expressed high level of M2-like signature genes, suggesting that it may play a role in driving ICC (Fig. 1B, S1B-C).

We further analyzed these six macrophage subtypes in human ICC by integrating two human ICC datasets (GSE138709[11] and GSE189903[12], Table S2). Interestingly, we found that Mφ_DNAJB1 was dominated in non-malignant tissues, different with its pattern in mouse (Fig. 1C-D, S1D). Further, we analyzed the correlation between macrophage subtypes and ICC prognosis using the Scissor algorithm[13], and found that

Mφ_SPP1 showed the strongest association with mortality among ICC patients in the GSE89749[14] and GSE107943[15] (Table S2, Fig. 1E). In addition, we selected the top 10 signature genes specifically highly expressed in the subtype Mφ_SPP1 (Table S4) and performed survival analyses. The results showed that patients with high expression of Mφ_SPP1 signatures (Mφ_SPP1 High) had significantly worse outcomes (Fig. 1E), further confirming the role of Mφ_SPP1 in the malignant progression of ICC.

We then conducted in-vivo experiments to validate the function of TAMs in ICC. We established ICC allografts by co-injection of BMDMs (Bone marrow-derived macrophages) with BR ICC cells (isolated from Bmi1/NRAS mouse ICC tissues). Flow cytometry analysis revealed an increased infiltration of $F4/80^{+}CD11b^{+}$ macrophages in the BR BMDM co-injection group, which was associated with a significant enhancement in tumor growth (Fig. 1F-G, S2). Next, we initiated intraperitoneal clodronate liposome treatment every three days starting on day 14 to deplete macrophages after hydrodynamic tail-vein injection of AKT1/NICD1 to induce ICC in mouse livers (Fig. 1H, S3). Macrophage depletion suppressed ICC progression, reflected by reduced liver tumor size (Fig. 1I). Moreover, macrophage infiltration ($CD11b^{+}F4/80^{+}$ within $CD45^{+}$ and $F4/80^{+}$ within $CD11b^{+}$) positively correlated with the liver-to-body weight ratio (Fig. 1I). Together, these findings indicate that TAMs in ICC is associated with malignant progression of ICC.

Mφ_SPP1 predominate from tumor boundary to the core and promote ICC progression

Considering the strong association of Mφ_SPP1 with malignant progression of ICC, we further validated its presence in the ICC patient using multiplex immunofluorescence (mIF). We observed a pronounced signal of $SPP1^{+}CD68^{+}$ macrophages at the periphery of $CK19^{+}$ ICC cells (Fig. 2A). Interestingly, $SPP1^{+}CD68^{+}$ macrophages showed the highest level of infiltration within 0 – 20 μm from the boundary of ICC nodules, indicating a potential s cell-cell interaction

between Mφ_SPP1 and ICC cells. Therefore, we further analyzed spatial transcriptomics to unravel the relation between Mφ_SPP1 and ICC progression. Using high-resolution 10x Visium HD assay and the BANKSY method [16], we identified seven cell types in human ICC tissues (Fig 2B, S5C). The results also showed the spatial proximity between the Mφ_SPP1 and ICC cells (Fig 2B, S5C). Moreover, Mφ_SPP1 showed evident co-occurrence with ICC cells and was predictive of the abundance of $CK19^{+}$ ICC cells by mistyR [17] (Fig. 2B).Next, using spatial transcriptomic data from human ICC tissues [18], we segmented ICC tissues into malignant, boundary, and non-malignant regions (Fig. 2C). Mφ_SPP1 scores (mean expression of the Mφ_SPP1 signatures) significantly increased from non-malignant to boundary regions, peaking in malignant regions (Fig. 2C). Kyoto encyclopedia of genes and genomes (KEGG) and gene ontology (GO) analysis indicated that genes related to cell cycle related pathway and epithelial-to-mesenchymal transition (EMT) were increased from the vicinity of ICC nodules to tumor boundary (Fig. 2C).

Next, we investigated the stimulatory roles of Mφ_SPP1 on ICC cells using multiple cell-cell co-culture systems is (Fig. S4A). We found that non-contact Transwell co-cultures of RAW264.7 cells or BMDMs with QBC939 or BR derived tumor-conditioned medium (TCM) generated TMAs with robust upregulation of *SPP1* and M2 markers including *ARG1*, *VEGFA*, *IL10* and *CD206*(Fig. S4B–F). EdU incorporation and migration assays demonstrated that macrophage co-culture significantly enhanced ICC cell proliferation (Fig. 2D) and migration, respectively (Fig. 2E). These results indicate that $SPP1^{+}$ macrophages promotes ICC cell proliferation and migration in an contact-independent manner.

Mφ_SPP1 promotes ICC proliferation via the OSM-OSMR-STAT3-CCND1 axis

To explore the mechanisms underlying Mφ_SPP1 mediated ICC progression, we re-clustered and obtained eight epithelial cell subpopulations from scRNAseq data of AKT1/NICD1 mouse ICC tissues (Fig. 3A). Among these cell populations, E_Alb was defined as hepatocytes and E_Fxyd2 as cholangiocytes, confirmed with lowest

CNV scores for non-malignancy (Fig. 3A, S5D). In contrast, E_Jun and E_Cd44 had the highest CNV scores and enriched proliferation-associated pathways including cell cycle, cell population proliferation and MAPK cascade, and cell invasion and metastasis related signaling including mesenchyme development and cell motility. These results indicate that E_Jun and E_Cd44 were ICC cell populations with high proliferative capacity and malignancy. Next, we integrated three cell-cell communication approaches (CellChat, CellphoneDB, NicheNet) to analyze interactions between Mφ_SPP1 and ICC cell population E_Jun and E_Cd44 in mice (Fig. 3B). Downstream signaling pathway analysis revealed that Mφ_SPP1 engages with ICC cells via *OSM* and *THBS1* ligands (Fig. 3B). Further analysis revealed that Osm and interacts with E_Cd44/E_Jun cells via receptor Osmr or Lifr (Fig. 3C-D, S6A). scRNAseq data from human ICC tissues also confirmed the communication between macrophage and cells via OSM/*OSMR* in (Fig. 3D, S6B). Spatial interaction analysis and spatial mapping by mIF further confirmed the co-localization of OSM^+ macrophages with $OSMR^+$ ICC cells (Fig 3E, S6C-E).

To identify the downstream signaling of OSM/OSMR and LIFR, we conducted NicheNet that software for target genes of ligand prediction and selected top 100 target genes regulated by OSM for further analysis. These genes were enriched in proliferation related pathways including JAK-STAT, Pi3K-AKT, mTOR and cell cycle pathways (Fig. 4A). To test whether *OSMR* and *LIFR* are required for ICC proliferation, we generated *Osmr*- or *Lifr*- liver conditional knockout mice $Osmr^{fl/fl}$; Alb-cre and $Lifr^{fl/fl}$; Alb-cre, and hydrodynamic injected them with AKT1/NICD1 or AKT1/YAP1 to induce ICC (Fig. 4B). Compared with $Lifr^{fl/fl}$ mice, $Lifr^{fl/fl}$; Alb-Cre mice showed no significant difference in liver-to-body weight ratio upon AKT1/NICD1 injection (Fig. 4C, S6F). However, $Osmr^{fl/fl}$; Alb-Cre mice exhibited a marked reduction of liver-to-body weight ratio after AKT1/NICD1 or AKT1/YAP1 injection compared with that in $Osmr^{fl/fl}$ mice (Fig. 4C, S7A). These results indicate that OSMR but not LIFR mediates the communication between Mφ_SPP1 and ICC cells.

Addition of recombinant OSM to ICC cell culture demonstrated that OSM increased

OSMR mRNA and protein levels and growth of ICC cells (Fig. 4B-E, S7B-C). OSM treatment or co-culture with BMDMs increased OSMR protein levels in mouse ICC cells (Fig. 4D). Similarly, RAW264.7 and QBC939 co-cultures increased mRNA levels of *OSM*, *VEGFA* and *IL10* in macrophages and *OSMR* mRNA levels in QBC939 cells (Fig. 4F, S7B). OSMR knockdown with siRNA suppressed ICC cell viability (Fig. S7E-F). Similarly, CRISPR-Cas9-mediated knockout of *OSMR* resulted in significantly decreased proliferation, viability, and clonogenicity of ICC cells (Fig. 4G-I, S7G-H).

We then analyzed downstream targets using phosphoproteomic and scRNAseq analysis. Upon recombinant OSM treatment, differentially phosphorylated proteins were enriched in PI3K-AKT, MAPK, and cell cycle related pathways (Fig. 5A). We obtained 37 genes through overlapping the top 100 *OSM* target genes from NicheNet with significantly highly expressed genes in ICC cells (Fig. 5B, Table S5). Subsequent protein interaction analysis revealed that Osmr was interacted with Stat3, and Stat3 was interacted with proliferation related genes *Myc* and *Ccnd1* (Fig. 5C). Notably, *Osmr* knockout did not reduce the number of infiltrated TAMs ($F4/80^+/CD206^+$) (Fig. 5D), but decreased the protein level of CCND1, BCL2, and p-STAT3 (Fig. 5F), indicating that OSM/OSMR activated these signaling in ICC cells. Taken together, these results demonstrate that OSM promotes ICC growth via OSMR and downstream CCND1, BCL2 and p-STAT3.

Mφ_SPP1 promotes ICC invasion via THBS1-CD47-mTOR/DBN1 axis

We then investigated the roles of THBS1 in ICC progression and found that THBS1 interacted with ICC cell via CD47 (Fig. 6A, S8A-B). Using NicheNet, we found that PI3K-Akt and EMT related genes were potential downstream signaling of *THBS1* in ICC cells (Fig. 6A). Critically, recombinant THBS1 treatment favored ICC cell growth marginally (Fig. S8C-D), but markedly enhanced migration of ICC cells (Fig. 6B-C). Correspondingly, *CD47* silencing significantly impaired the stimulatory effects of THBS1 in promoting ICC cell migration (Fig. 6D). Co-culture with BMDMs promoted BR migration ability, whereas *Cd47* knockdown blocked this

effect (Fig. 6E, S8E). Similarly, *Cd47* silencing inhibited subcutaneous allograft progression in mice (Fig. 6F, S8F-G). Moreover, *Cd47* knockdown markedly suppressed ICC dissemination in a peritoneal metastasis mouse model, as evidenced by reduced metastatic nodule formation and decreased ascites accumulation (Fig. 6G, S8H). Consistently, CD47 silencing attenuated local invasion into the surrounding hepatic parenchyma in the orthotopic ICC injection mouse model (Fig. 6G).

To further elucidate the downstream molecules of *THBS1* in promoting ICC migration, we treated HuCCT1 cells with THBS1 and collected cells at different time points. Western blotting showed that recombinant THBS1 induced rapid induction of p-mTORC1, p-RPS6 and EMT related proteins at 10 min with a peak at 2 h (Fig. 7A, S9A). Phosphoproteomics analysis of HuCCT1 cells treated with recombinant THBS1 at 0, 2, and 12 h revealed elevated phosphorylation of PI3K-AKT and EMT related signaling proteins at 2 h (Fig. 7B). In comparison, differential protein phosphorylation was enriched in cell adhesion pathways at 12 h (Fig. 7B, S9B). Ranking differentially phosphorylated sites by fold change (2 h vs 0 h) identified DBN1 Ser142 as the most strongly upregulated phosphorylation site at 2 h (Fig. 7C). These results suggest that mTORC1 and DBN1 signaling medicate the role of THBS1/CD47 in favoring ICC migration.

Next, we examined their roles in enabling ICC migration through co-culture of ICC cells with BMDM, and found that *Thbs1* in BMDMs and p-mTORC1 (Ser142) Vimentin and, p-DBN1 in ICC cells were fundamentally increased (Fig. 7D, S9C-D). Inhibition of mTORC1 by rapamycin substantially suppressed the pro-migratory effect of BMDMs on ICC cells (Fig. 7E) and completely abrogated the THBS1 induced migration (Fig. 7F), indicating that THBS1 promotes ICC cell migration via mTORC1 activation. Likewise, inhibition of DBN1 with its inhibitor BTP2 significantly blocked the migration of ICC cells (Fig. 7G). Notably, BTP2 decreased phosphorylation at Ser142 of DBN1 (Fig.7H). Together, these results demonstrate the critical roles of p-mTORC1 and p-DBN1(Ser142) phosphorylation in THBS1 mediated ICC cell migration.

Finally, we examined the role of THBS1 in sgP19/KRAS induced metastatic ICC

346 mouse model with Thbs1$^{fl/fl}$; Lyz-Cre mice (Fig. 7I). Myeloid-specific knockout of
347 *Thbs1* significantly reduced liver-to-body weight ratios and tumor burden and
348 markedly suppressed peripheral metastasis of ICC to multiple distant organs,
349 including the intestines, lungs, lymph nodes, kidneys, and diaphragm (Fig. 7I-J).
350 Furthermore, western blotting of ICC tissues revealed that metastasis related CD47,
351 DBN1, p-DBN1 (Ser142), p-mTORC1, and Vimentin levels were significantly
352 downregulated after *Thbs1* deletion (Fig. 7K). Collectively, these findings corroborate
353 that THBS1 promotes ICC metastasis via PI3K-AKT-mTOR activation and DBN1
354 phosphorylation.

355 **Blockade of OSM and THBS1 synergistically inhibits ICC progression**

356 As *OSM* promotes ICC cell proliferation and *THBS1* enhances invasiveness, we
357 examined whether dual inhibition could synergistically suppress ICC. We analyzed
358 *THBS1* and *OSM* expression in ICC tissues from 827 samples of nine
359 ICC/cholangiocarcinoma cohorts (Table S2) and calculated mean expression levels of
360 *THBS1* and *OSM* in each cohort. An ICC sample was defined as double positive if
361 both genes had expression levels greater than the mean value of the cohort. Across the
362 nine datasets, the proportion of ICC samples co-expressing *THBS1* and *OSM* ranged
363 from 13.33% to 29.53%, and those in in five datasets exceeded 20% (Fig. 8A).
364 Prognostic analyses across three datasets showed that patients with high expression of
365 both *OSM* and *THBS1* had significantly shorter overall survival (Fig. 8B).

366 Next, we genetically ablated macrophage derived *THBS1* using Thbs1$^{fl/fl}$; Lyz-cre
367 mice and pharmacologically inhibited OSM-OSMR interaction via intraperitoneal
368 administration of OSM-SMI-10B, an OSMR inhibitor.[19] *Thbs1* deletion or *Osmr*
369 inhibition alone suppressed ICC progression moderately, while combined blockade
370 attenuated ICC development more robustly, as evidenced by further reduced tumor
371 burden using H&E staining and a decreased liver-to-body weight ratio (Fig. 8C–E).
372 These results collectively indicate that combined blockade of OSM and THBS1 may
373 generate synergetic therapeutic effects for ICC treatment. Finally, we validated the
374 spatial proximity relationship between OSM^{+}THBS1^{+}SPP1^{+} and CK19^{+} cells using

375 mIF (Fig. 8F). The results showed that $OSM^{+}THBS1^{+}CD68^{+}SPP1^{+}$ cells were
376 spatially adjacent to $CK19^{+}$ cells (Fig. 8F), and OSM^{+} and $THBS1^{+}$ were
377 co-expressed in $CD68^{+}$ cells (Fig. 8F). Patients with high $OSM^{+}THBS1^{+}$
378 co-expression were associated with significantly worse survival (Fig. 8F). These
379 findings suggest that macrophage-derived OSM and THBS1 represent promising
380 therapeutic targets in a substantial subset of patients with ICC.
381

Discussion

The roles of TAMs in ICC have been linked to poor prognosis through promotion of tumor growth and invasiveness.[20, 21] Recent single-cell omics studies have revealed the molecular diversity and functions of TAMs in cancer,[22] but the specific subgroups driving ICC malignancy and its interactions with tumor cells remain unclear. Using a time resolved ICC mouse model with integrated multi omics, we identified Mφ_SPP1 as a poor prognosis TAM subset in ICC. The prognostic significance of Mφ_SPP1 was also observed in hepatocellular carcinoma (HCC),[23] underscoring its prevalence across liver cancers.[24]

Moreover, our study uncovers mechanism underlying Mφ_SPP1 to promote ICC progression or metastasis instead of suppressing tumor immune microenvironment. Mφ_SPP1 promotes ICC cell proliferation through OSM-OSMR and downstream p-STAT3 and CCND1. This observation is consistent with the findings that OSM promotes cancer cell proliferation in glioblastoma [25] and pancreatic ductal adenocarcinoma.[26] Differently, Mφ_SPP1 exerts tits pro-invasive role through secreted THBS1 to activate CD47 signaling in ICC cells. THBS1 has been reported releasing from tumor infiltrating monocyte-like cells and inducing an immunosuppressive TME to boost metastasis.[27] Instead, we demonstrate that *CD47* activates mTOR and DBN1 in ICC cells but not IL6/STAT3, leading to EMT and cell skeleton remolding.[28]

Last, our findings offer a new therapeutic strategy for ICC treatment by aiming at molecules derived from Mφ_SPP1. Mφ_SPP1 secrets OSM and THBS1 to accelerate ICC growth and metastasis via OSMR and CD747, respectively. Combined blockades of OSM-OSMR and THBS1-CD47 signaling led to retarded growth and restrained metastasis in primary ICC mouse models, while single inhibition generated modest efficacy. Consistently, a clinical trial showed that targeting OSM-OSMR signaling alone led to poor outcomes or drug resistance.[29] In addition, OSM and THBS1 were

concurrently upregulated in 13–29% of patients with ICC. Thus, targeting dual modulators of Mφ_SPP1 provides a potentially more robust therapeutic option for those patients with ICC.

References

[1] Moris D, Palta M, Kim C, Allen PJ, Morse MA, Lidsky ME. Advances in the treatment of intrahepatic cholangiocarcinoma: An overview of the current and future therapeutic landscape for clinicians. CA: a cancer journal for clinicians 2023;73:198-222.

[2] Greten TF, Schwabe R, Bardeesy N, Ma L, Goyal L, Kelley RK, et al. Immunology and immunotherapy of cholangiocarcinoma. Nat Rev Gastroenterol Hepatol 2023;20:349-365.

[3] Zhou M, Wang C, Lu S, Xu Y, Li Z, Jiang H, et al. Tumor-associated macrophages in cholangiocarcinoma: complex interplay and potential therapeutic target. EBioMedicine 2021;67:103375.

[4] Guan F, Wang R, Yi Z, Luo P, Liu W, Xie Y, et al. Tissue macrophages: origin, heterogenity, biological functions, diseases and therapeutic targets. Signal Transduct Target Ther 2025;10:93.

[5] Chen S, Saeed A, Liu Q, Jiang Q, Xu H, Xiao GG, et al. Macrophages in immunoregulation and therapeutics. Signal Transduct Target Ther 2023;8:207.

[6] Fan G, Tao C, Li L, Xie T, Tang L, Han X, et al. The co-location of MARCO+ tumor-associated macrophages and CTSE+ tumor cells determined the poor prognosis in intrahepatic cholangiocarcinoma. Hepatology 2025;82:25-41.

[7] Song G, Shi Y, Meng L, Ma J, Huang S, Zhang J, et al. Single-cell transcriptomic analysis suggests two molecularly subtypes of intrahepatic cholangiocarcinoma. Nat Commun 2022;13:1642.

[8] Zuyin L, Zhao L, Qian C, Changkun Z, Delin M, Jialing H, et al. Single-Cell and Spatial Transcriptomics Delineate the Microstructure and Immune Landscape of Intrahepatic Cholangiocarcinoma in the Leading-Edge Area. Advanced science (Weinheim, Baden-Wurttemberg, Germany) 2024:e2412740.

[9] Yan J, Jiang Z, Zhang S, Yu Q, Lu Y, Miao R, et al. Spatial–temporal heterogeneities of liver cancer and the discovery of the invasive zone. Clin Transl Med 2025;15:e70224.

[10] Dong LQ, Shi Y, Ma LJ, Yang LX, Wang XY, Zhang S, et al. Spatial and temporal clonal evolution of intrahepatic cholangiocarcinoma. J Hepatol 2018;69:89-98.

[11] Zhang M, Yang H, Wan L, Wang Z, Wang H, Ge C, et al. Single-cell transcriptomic architecture and intercellular crosstalk of human intrahepatic cholangiocarcinoma. J Hepatol 2020;73:1118-1130.

[12] Ma L, Heinrich S, Wang L, Keggenhoff FL, Khatib S, Forgues M, et al. Multiregional single-cell dissection of tumor and immune cells reveals stable lock-and-key features in liver cancer. Nat Commun 2022;13:7533.

[13] Sun D, Guan X, Moran AE, Wu L-Y, Qian DZ, Schedin P, et al. Identifying phenotype-associated subpopulations by integrating bulk and single-cell sequencing data. Nature Biotechnology 2021;40:527-538.

[14] Jusakul A, Cutcutache I, Yong CH, Lim JQ, Huang MN, Padmanabhan N, et al. Whole-Genome and Epigenomic Landscapes of Etiologically Distinct Subtypes of Cholangiocarcinoma. Cancer Discov 2017;7:1116-1135.

[15] Ahn KS, O'Brien D, Kang YN, Mounajjed T, Kim YH, Kim TS, et al. Prognostic subclass of intrahepatic cholangiocarcinoma by integrative molecular-clinical analysis and potential targeted approach. Hepatol Int 2019;13:490-500.

[16] Singhal V, Chou N, Lee J, Yue Y, Liu J, Chock WK, et al. BANKSY unifies cell typing and tissue domain segmentation for scalable spatial omics data analysis. Nat Genet 2024;56:431-441.

[17] Tanevski J, Flores ROR, Gabor A, Schapiro D, Saez-Rodriguez J. Explainable multiview framework for dissecting spatial relationships from highly multiplexed data. Genome Biol 2022;23:97.
[18] Wu R, Guo W, Qiu X, Wang S, Sui C, Lian Q, et al. Comprehensive analysis of spatial architecture in primary liver cancer. Sci Adv 2021;7:eabg3750.
[19] Wolf CL, Feci A, Tuccinardi JP, Coughlin GH, Holdaway KA, Muhammed T, et al. Development of the First Small-Molecule Inhibitor Targeting Oncostatin M for Treatment of Breast Cancer. J Med Chem 2025;68:15422-15445.
[20] Hasita H, Komohara Y, Okabe H, Masuda T, Ohnishi K, Lei XF, et al. Significance of alternatively activated macrophages in patients with intrahepatic cholangiocarcinoma. Cancer science 2010;101:1913-1919.
[21] Yuan H, Lin Z, Liu Y, Jiang Y, Liu K, Tu M, et al. Intrahepatic cholangiocarcinoma induced M2-polarized tumor-associated macrophages facilitate tumor growth and invasiveness. Cancer cell international 2020;20:586.
[22] Ma RY, Black A, Qian BZ. Macrophage diversity in cancer revisited in the era of single-cell omics. Trends Immunol 2022;43:546-563.
[23] Zhang Q, He Y, Luo N, Patel SJ, Han Y, Gao R, et al. Landscape and Dynamics of Single Immune Cells in Hepatocellular Carcinoma. Cell 2019;179:829-845.e820.
[24] Okikawa S, Morine Y, Saito Y, Yamada S, Tokuda K, Teraoku H, et al. Inhibition of the VEGF signaling pathway attenuates tumor-associated macrophage activity in liver cancer. Oncology reports 2022;47.
[25] Chen M, Ren R, Lin W, Xiang L, Zhao Z, Shao B. Exploring the oncostatin M (OSM) feed-forward signaling of glioblastoma via STAT3 in pan-cancer analysis. Cancer cell international 2021;21:565.
[26] Polak KL, Tamagno I, Parameswaran N, Smigiel J, Chan ER, Yuan X, et al. Oncostatin-M and OSM-Receptor Feed-Forward Activation of MAPK Induces Separable Stem-like and Mesenchymal Programs. Molecular cancer research : MCR 2023;21:975-990.
[27] Omatsu M, Nakanishi Y, Iwane K, Aoyama N, Duran A, Muta Y, et al. THBS1-producing tumor-infiltrating monocyte-like cells contribute to immunosuppression and metastasis in colorectal cancer. Nature communications 2023;14:5534.
[28] You Y, Tian Z, Du Z, Wu K, Xu G, Dai M, et al. M1-like tumor-associated macrophages cascade a mesenchymal/stem-like phenotype of oral squamous cell carcinoma via the IL6/Stat3/THBS1 feedback loop. J Exp Clin Cancer Res 2022;41:10.
[29] Wolf CL, Pruett C, Lighter D, Jorcyk CL. The clinical relevance of OSM in inflammatory diseases: a comprehensive review. Front Immunol 2023;14:1239732.

Supplementary Material

To access the supplementary material accompanying this article, visit the online version.

Figures

Fig. 1. Mφ_SPP1 is enriched in ICC and is associated with poor prognosis. (A) UMAP plot visualization of cell types in AKT1/NICD1 mouse ICC tissues. (B) UMAP plot visualizes macrophage cell types in AKT1/NICD1 mouse ICC tissues (left). Bubble plots display the expression of macrophage marker genes in the AKT1/NICD1 mice. Color indicates expression levels; bubble size reflects cell proportion (middle). Heatmap illuminates tissue infiltration of macrophage subtypes (right). (C) UMAP plot visualizes cell types in human ICC tissues. (D) UMAP plot visualizes macrophage subtypes in human ICC tissues (left). Bubble plots display the expression of macrophage marker genes in the human ICC tissues (right first row). Heatmap illuminates tissue infiltration of macrophage subtypes (right second row). (E) Scatter-pie (the left two) and plots illustrate prognostic associations of distinct macrophage subtypes. Pie chart illustrates cell prognosis outcomes in each macrophage subtype. Blue, survival; red, death; grey, no significant association. Prognosis (the right two) of Mφ_SPP1- high and Mφ_SPP1- low patients in two bulk RNA data sets (GSE89749 and GSE107943). Statistical significance was calculated using the log- rank test. (F) Schematic of the co-injection experiment. A mixture of bone marrow-derived macrophages (BMDMs) and BR cells (1:1 ratio) was inoculated subcutaneously into one flank of mice to mimic macrophage infiltration, while BR cells alone were injected into the contralateral flank as a control. Quantification of tumor-infiltrating macrophages ($F4/80^{+}CD11b^{+}$ cells) by flow cytometry. Data are presented as mean ± SD; Significance was determined by a two-tailed unpaired t-test. $^{**}p < 0.01$, and n = 4 mice. (G) Subcutaneous co-injection tumor model experiments were performed to validate the role of macrophage infiltration in ICC progression. BR group: injection of BR primary cells alone. BR+BMDM group: co-injection of BR primary cells with BMDM. From left to right, representative photographs of xenograft tumors, tumor volume growth curves (in units of 1,000 mm^3), and tumor weights are shown. (H) Schematic illustration of the macrophage depletion strategy in AKT1/NICD1 ICC mouse model. The AKT1/NICD1 ICC mouse model was established on Day 0 via hydrodynamic tail vein injection of AKT1 and NICD1 plasmids. From Day 14 onwards, clodronate liposomes or control liposomes were administered intraperitoneally every 3 days. All mice were sacrificed, and ICC tissues were collected and analyzed on Day 31. (I) In the AKT1/NICD1-driven ICC mouse model, macrophage depletion was achieved via

clodronate liposome injection to investigate its impact on ICC progression. The control group received neutral control liposomes. Left: representative liver images; right: macrophage infiltration levels (R1, $CD11b^+F4/80^+$ cells within $CD45^+$ population; R2, $F4/80^+$ cells within $CD11b^+$ population), analyzed via flow cytometry and correlated with liver-to-body weight ratio using scatter plots. Correlation analysis was performed using Spearman's rank correlation test.

Fig2. Mφ_SPP1 is spatially proximal to ICC cells and promotes ICC malignant progression. (A) Multiplex immunofluorescence (mIF) demonstrating dense infiltration of $SPP1^+CD68^+$ macrophages surrounding $CK19^+$ cells (left). Heatmap of tissue spatial infiltration patterns for ICC cells ($CK19^+$) (highlighted in yellow) in a representative ICC sample (middle). Bar plots showing the proportion of $SPP1^+CD68^+$ cells at different distance bins from $CK19^+$ ICC cells in two validation datasets (right). (B) Spatial domains defined by BANKSY in the ICC patient dataset using the 10x HD platform (the first). Cell type composition across the spatial domains (the second). Spatial proximity between Mφ_SPP1 and ICC cells (the third). Median importance of cell type abundance in the prediction of abundances of other cell types in the local niche view (the fourth). (C) H&E of human ICC tissue (the first). Spatial segmentation of ICC tissues (the second). Violin plots show the spatial distribution of Mφ_SPP1 cells and the spatial enrichment of malignant functions in ICC cells across the tissue. (D) Fluorescence microscopy images of EdU incorporation assays in HuCCT1, RBE, and QBC939 cells transwell co-cultured with BMDMs. Scale bar = 50 μm. (E) Quantification of EdU positive rate from the experiment shown in (A). Data are presented as mean ± SD. Significance was determined by a two-tailed unpaired t-test (***$p < 0.001$, ****$p < 0.0001$, and n = 4 independent experiments). (F) Representative crystal violet–stained images of Transwell migration assays for BR and HuCCT1 cells cultured alone or co-cultured with BMDMs.

Fig. 3. Mφ_SPP1 interacts with ICC cells via OSM-OSMR. (A) UMAP plot (left) and box plot (middle) illustrate the CNV scores of epithelial subtypes in AKT1/NICD1. Bubble chart visualizing pathway enrichment results for the subtypes E_Jun and E_Cd44 with the highest CNV scores (right). (B) Venn diagram showing overlap of ligand genes significantly upregulated in Mφ_Spp1 (mouse, Mouse_TAM_diff) and Mφ_SPP1 (human, Human_TAM_Diff), which exhibit

559 strong interactions with tumor cells, as identified by three cell communication methods
560 (CellphoneDB, CellChat and NicheNet). (C) Heatmap showing the interaction intensity of *OSM*
561 signaling between macrophage and ICC cells in AKT1/NICD1 mouse ICC tissues. (D) Violin
562 plots show *Osm* in macrophage and its receptor *Osmr* expression in epithelial subtypes in mouse
563 tissues (left). Scatter plots show the OSM-OSMR gene pair in human ICC single cell and spatial
564 RNAseq data. (E) Multiplex immunofluorescence showing spatial co-localization between
565 $CD68^{+}OSM^{+}$ TAMs and $OSMR^{+}KRT19^{+}$ ICC cells in patients with ICC. Scale bar, 200 μm.
566
567 **Fig. 4. Mφ_SPP1 promotes ICC proliferation by in ICC cells via OSM-OSMR.** (A) Bar plot
568 showing the top KEGG pathways of Osm target genes obtained by NicheNet. (B) Representative
569 images of livers from $Lifr^{fl/fl}$ and $Osmr^{fl/fl}$ control mice and $Lifr^{fl/fl}$; Alb-Cre and $Osmr^{fl/fl}$; Alb-Cre
570 mice injected with AKT1/NICD1. (C) Liver-to-body weight ratios Western blot results (i) and
571 CCK-8 assay (ii) for cell viability measurements of HuCCT1 and QBC939 cells treated with 2.5
572 ng/mL or 5.0 ng/mL OSM or untreated cells for 5 consecutive days. Western blot results (D) and
573 CCK-8 assay (E) for cell viability measurements of HuCCT1 and QBC939 cells treated with 2.5
574 ng/mL or 5.0 ng/mL OSM or untreated cells for 5 consecutive days. (F) Bar plot showing gene
575 expression levels in co-culture. Statistical significance was analyzed using one-way ANOVA ($p <$
576 0.05), followed by Dunnett's test (ns, not significant, $^{**}p < 0.01$, $^{***}p < 0.001$; $^{****}p < 0.0001$).
577 (G) EdU incorporation assay in QBC939 cells transduced with control vector or OSMR-targeting
578 sgRNAs (sgOSMR-1, sgOSMR-2). Scale bar, 200 μm. (H) CCK-8 assay for viability
579 measurements of HuCCT1 and QBC939 cells transduced with control vector or sgOSMR-1 at
580 days 1, 3, and 5 after seeding. (I) Colony formation assay with crystal violet staining of HuCCT1
581 and QBC939 cells transduced with control vector or sgOSMR-1.
582
583 **Fig. 5. Mφ_SPP1 promotes ICC proliferation by upregulating p-STAT3 and CCND1 in ICC**
584 **cells.** (A) Bar plot showing KEGG pathway enrichment among phosphorylated proteins after
585 OSM treatment in QBC939 cells. Blue, downregulation; red, upregulation. (B) Venn plot shows
586 the candidate target genes of Osm. (C) Protein network showing the candidate signaling of
587 Osm-Osmr. (D) Immunohistochemical staining of $CD206^{+}$ and $F4/80^{+}$ in paraffin-embedded liver
588 sections from $Osmr^{fl/fl}$ and $Osmr^{fl/fl}$;Alb-Cre mice injected with AKT1/NICD1. Scale bars

represent 50 μm. (E) qRT-PCR analysis of *MYC* transfected with OSM recombinant protein or siScramble/siOSMR sequences in QBC939 cells. Data are presented as mean ± SD. Statistical significance was analyzed by a two-tailed unpaired t-test (****$p < 0.0001$, n = 3 independent experiments). (F) Western blot analysis of OSMR, CCND1, BCL2, phosphorylated STAT3 (p-STAT3), phosphorylated mTORC1 (p-mTORC1), and OSM protein levels, with GAPDH serving as a loading control, in $Osmr^{fl/fl}$ and $Osmr^{fl/fl}$; Alb-Cre mice injected with AKT1/NICD1.

Fig. 6. Mφ_SPP1 promotes ICC invasion via THBS1-CD47 signaling. (A) (i) Heatmap of interactions between Mφ_Spp1 and tumor subtypes in THBS1 signaling (left). Bar plot showing the top KEGG pathways and hallmark gene sets of Thbs1 target genes obtained by NicheNet. (B) Representative scratch-wound images of HuCCT1 and RBE cells with or without 10 ng/mL THBS1 or control. HuCCT1 at 0, 12, and 24 h; RBE at 0, 36, and 72 h. Scale bar, 150 μm. (C) Representative crystal violet-stained Transwell migration images of primary BR cells and HuCCT1 cells treated with 10 ng/mL THBS1 or control. Scale bar, 150 μm. (D) qRT-PCR analysis of *CD47* levels in HuCCT1 cells transfected with siScramble control, siCD47-1, or siCD47-2 for 48 h. Data are presented as mean ± SD. Statistical significance was analyzed by one-way ANOVA ($p < 0.05$) followed by Dunnett's test (****$p < 0.0001$)(left first row). Representative crystal violet-stained Transwell migration images of HuCCT1 cells transfected with siScramble or siCD47. Scale bar, 150 μm (left second row). Quantification of cell migration area by ImageJ in Transwell assays of HuCCT1 cells transfected with siScramble or siCD47-2, seeded in the upper chamber. The lower chamber contained either complete medium or Thbs1-supplemented complete medium. Data are presented as mean ± SD. Statistical significance was analyzed by one-way ANOVA ($p < 0.05$) followed by Dunnett's test (****$p < 0.0001$). (right). (E) qRT-PCR (the first row) and western blot (the second row) analyses of CD47 transcript and protein levels, respectively, in BR cells transduced with LV3-shNC control entivirus or LV3-shCD47.(F) Representative crystal violet-stained Transwell migration images and corresponding chamber images of BR cells transduced with LV3-shNC or LV3-shCd47 co-cultured with BMDMs or cultured with complete medium for 24 h. Scale bar, 150 μm. (G) Subcutaneous allograft ICC growth curves and representative ICC tissue images (left) of BR cells transduced with LV3-shNC or LV3-shCd47 lentivirus (right). (H) Representative photographs of

619 mice following intraperitoneal injection of LV3-shNC (n = 3 mice) or LV3-shCd47 infected BR
620 cells (n = 5 mice) (left). Representative images of mouse abdominal phenotypes at tumor endpoint
621 after intraperitoneal injection of BR cells transduced with LV3-shNC or LV3-shCd47 (right). (I)
622 Quantification of metastatic nodules and volume of ascites collected (first row). Representative
623 images mouse livers from mice with orthotopic liver injection. Both groups were injected with
624 equal amounts of BR shNC or BR shCD47 cells into the left liver lobe (second row).
625
626 **Fig. 7. Mφ_SPP1 promotes ICC invasion via activated mTORand phosphorylated DBN1.** (A)
627 Western blotting showing the expression of p-mTOR, p-RPS6, EpCAM, N-cadherin, Vimentin,
628 and the internal control GAPDH in HuCCT1 cells after recombinant THBS1 stimulation. (B) Bar
629 plot displaying pathway enrichment analysis for HuCCT1 at 6 and 2 h following the addition of
630 exogenous THBS1 protein. (C) Circos plot displaying differentially phosphorylated sites at
631 multiple time points after adding exogenous THBS1. From inner to outer rings:
632 phosphorylation-site proportions, phosphopeptide expression intensity (inner heatmap), sample
633 groups, and enriched signaling pathways; the outermost ring lists gene symbols and phosphosites
634 unique to each treatment. Colored links show shared phosphosites: gray, common to control and
635 treatments; brown, mTOR-related; red, fibrosis-related; green, mesenchymal-related. Large and
636 small ticks denote 50 and 5 phosphopeptides, respectively. (D) Western blot analysis of DBN1,
637 phosphorylated DBN1 (p-DBN1, Ser142), and Vimentin protein levels in BR cells cultured alone
638 or co-cultured with BMDMs for 24 h or 48 h; GAPDH served as a loading control. (E)
639 Representative crystal violet-stained images from Transwell migration assays of HuCCT1 and BR
640 cells co-cultured with BMDMs, with or without rapamycin treatment. N = 5. Scale bar, 200 μm. (F)
641 Representative crystal violet-stained images from Transwell migration assays of HuCCT1 and BR
642 cells treated with THBS1, with or without rapamycin blockade; groups include control, THBS1
643 treatment, and THBS1 combined with rapamycin. N = 5. Scale bar, 200 μm. (G) Representative
644 chamber and crystal violet-stained images from Transwell migration assays for HuCCT1 cells (left)
645 treated with 0, 5, 25, and 125 μM BTP2 inhibitor, and BR cells (right) treated with 0, 25, and 125
646 μM BTP2 in the lower chamber. Scale bar, 200 μm. (H) Western blot analysis of p-DBN1
647 (Ser142), p-mTORC1 (Ser2448), Vimentin, and CD47 protein levels in RBE cells treated with 50
648 μm BTP2 for 24 h. GAPDH was used as a loading control. (I) Representative images of metastatic

ICC lesions from various organs in Thbs1$^{fl/fl}$; Lyz-Cre and Thbs1$^{fl/fl}$ mice injected with sgP19/KRAS. Scale bars: 1 cm for liver; 5 mm for lung, spleen, kidney, peritoneum, and colon (first row). H&E, CK19, and Ki67 staining of metastatic tumor nests in sections from different organs in Thbs1$^{fl/fl}$; Lyz-Cre and Thbs1$^{fl/fl}$ mice injected with sgP19/KRAS. This lymph node is referred to as the largest lymph node adjacent to the spleen. Scale bar, 200 μm (second row). (J) Metastatic nodule numbers in the sgP19/KRAS ICC metastasis model. Data are presented as mean ± SD. Significance was determined by a two-tailed unpaired t-test (***$p < 0.001$). (K) Western blot analysis of DBN1, CD47, p-mTORC1(Ser2448), and Vimentin protein expression in tumor tissues from Thbs1$^{fl/fl}$; Lyz-Cre and Thbs1$^{fl/fl}$ mice injected with sgP19/KRAS; GAPDH served as loading control.

Fig. 8. Combined intervention with OSM inhibitor and THBS1 knockout effectively delays ICC progression. (A) Stacked bar plot illustrating the prevalence of OSM$^+$THBS1$^+$ dual positive patients within distinct ICC cohorts. (B) High (red) and low (green) groups were defined by the mean expression of OSM and THBS1, respectively; survival in three datasets was compared using the log-rank test (Merge, GSE107943, GSE244807, and E-MTAB–6389). (C) Representative liver images from four experimental groups in the *THBS1/OSM* combination blockade experiment: (1) Thbs1$^{fl/fl}$ + vehicle control; (2) Thbs1$^{fl/fl}$ + OSM-SMI-10B; (3) Thbs1$^{fl/fl}$; Lyz2-Cre + vehicle control; (4) Thbs1$^{fl/fl}$; Lyz2-Cre + OSM-SMI-10B. (D) Statistical analysis of liver-to-body weight ratio across different treatment groups in the *THBS1/OSM* combination blockade experiment. Data are presented as mean ± SD. Statistical significance was analyzed using one-way ANOVA ($p < 0.05$), followed by Dunnett's test (*$p < 0.05$, **$p < 0.01$, ***$p < 0.001$; ****$p < 0.0001$). (E) H&E and IHC staining of liver sections from the *THBS1/OSM* combination blockade experiment. Ki67 and Ck19 positively identify ICC tumor nest regions. Scale bar, 200 μm. (F) (i) Proximity of OSM$^+$THBS1$^+$CD68$^+$SPP1$^+$ cells to CK19$^+$ cells by mIF. yellow, CK19$^+$; orange-red/green/blue, 0–20, 20–40, 40–60 μm from CK19$^+$. (ii) mIF shows OSM$^+$THBS1$^+$CD68$^+$SPP1$^+$ macrophages around CK19$^+$ cells. (iii) Spearman correlation between OSM$^+$THBS1$^+$ and CD68$^+$ intensity. (iv) Patients stratified by OSM$^+$ and THBS1$^+$ intensity (red = OSM$^+$THBS1$^+$ high, green = OSM$^+$THBS1$^+$ low); survival compared using log-rank test.

Figure 1

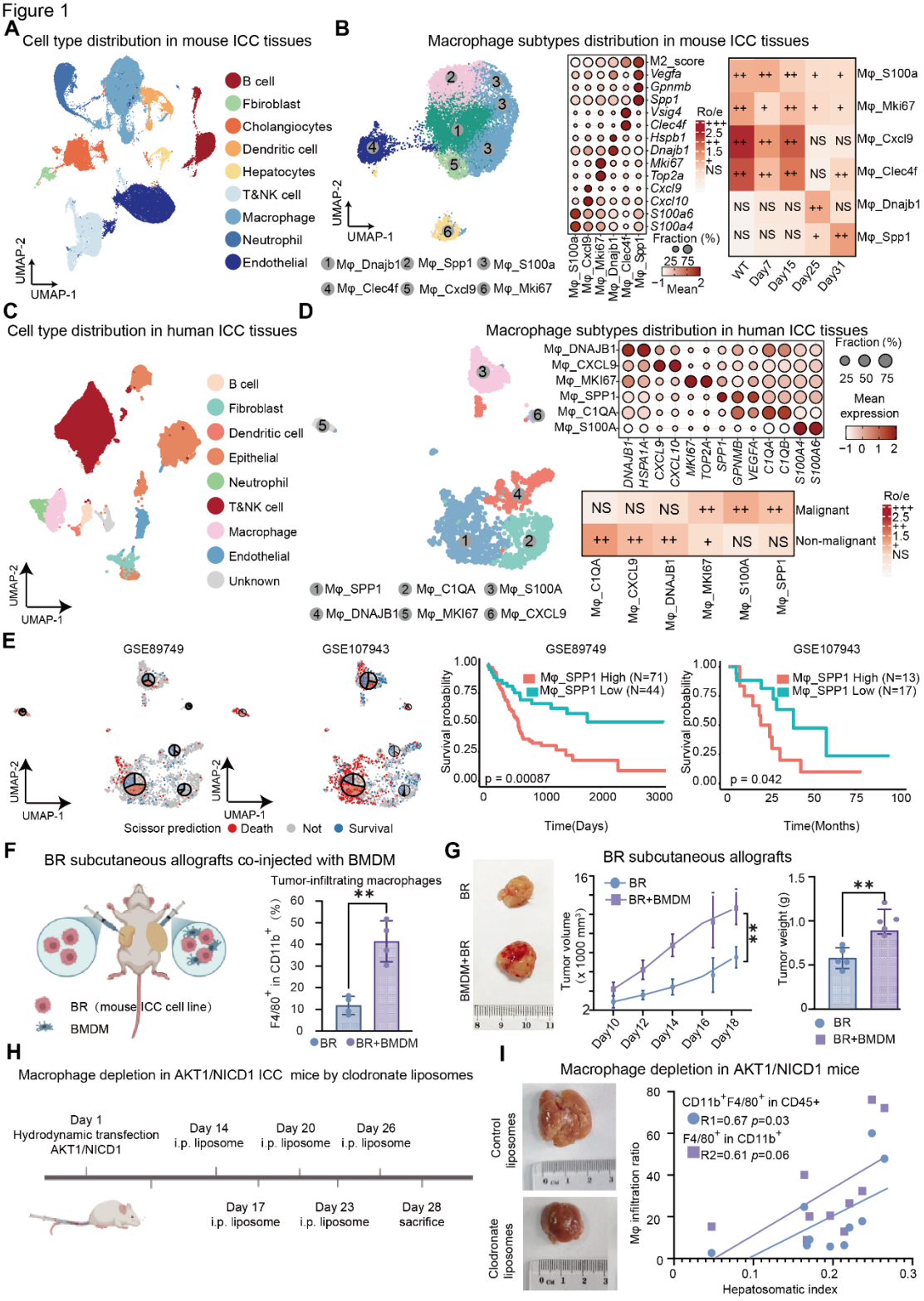
A
Cell type distribution in mouse ICC tissues
B cell
Fbiroblast
Cholangiocytes
Dendritic cell
Hepatocytes
T&NK cell
Macrophage
Neutrophil
Endothelial
UMAP-2
UMAP-1
B
Macrophage subtypes distribution in mouse ICC tissues
1 Mφ_Dnajb1 2 Mφ_Spp1 3 Mφ_S100a
4 Mφ_Clec4f 5 Mφ_Cxcl9 6 Mφ_Mki67
M2_score
Vegfa
Gpnmb
Spp1
Vsig4
Clec4f
Hspb1
Dnajb1
Mki67
Top2a
Cxcl9
Cxcl10
S100a6
S100a4
Fraction (%)
Mean
Ro/e
NS
Mφ_S100a
Mφ_Mki67
Mφ_Cxcl9
Mφ_Clec4f
Mφ_Dnajb1
Mφ_Spp1
WT
Day7
Day15
Day25
Day31
C
Cell type distribution in human ICC tissues
B cell
Fibroblast
Dendritic cell
Epithelial
Neutrophil
T&NK cell
Macrophage
Endothelial
Unknown
D
Macrophage subtypes distribution in human ICC tissues
1 Mφ_SPP1 2 Mφ_C1QA 3 Mφ_S100A
4 Mφ_DNAJB1 5 Mφ_MKI67 6 Mφ_CXCL9
Mφ_DNAJB1
Mφ_CXCL9
Mφ_MKI67
Mφ_SPP1
Mφ_C1QA
Mφ_S100A
DNAJB1
HSPA1A
CXCL9
CXCL10
MKI67
TOP2A
SPP1
GPNMB
VEGFA
C1QA
C1QB
S100A4
S100A6
Malignant
Non-malignant
E
GSE89749
GSE107943
Scissor prediction Death Not Survival
Mφ_SPP1 High (N=71)
Mφ_SPP1 Low (N=44)
p = 0.00087
Survival probability
Time(Days)
Mφ_SPP1 High (N=13)
Mφ_SPP1 Low (N=17)
p = 0.042
Time(Months)
F
BR subcutaneous allografts co-injected with BMDM
BR (mouse ICC cell line)
BMDM
Tumor-infiltrating macrophages
F4/80+ in CD11b+ (%)
BR
BR+BMDM
G
BR subcutaneous allografts
BMDM+BR
Tumor volume (x 1000 mm³)
Tumor weight (g)
Day10
Day12
Day14
Day16
Day18
H
Macrophage depletion in AKT1/NICD1 ICC mice by clodronate liposomes
Day 1
Hydrodynamic transfection
AKT1/NICD1
Day 14
i.p. liposome
Day 20
i.p. liposome
Day 26
i.p. liposome
Day 17
i.p. liposome
Day 23
i.p. liposome
Day 28
sacrifice
I
Macrophage depletion in AKT1/NICD1 mice
Control liposomes
Clodronate liposomes
CD11b+F4/80+ in CD45+
R1=0.67 p=0.03
F4/80+ in CD11b+
R2=0.61 p=0.06
Mφ infiltration ratio
Hepatosomatic index

679

Figure 2

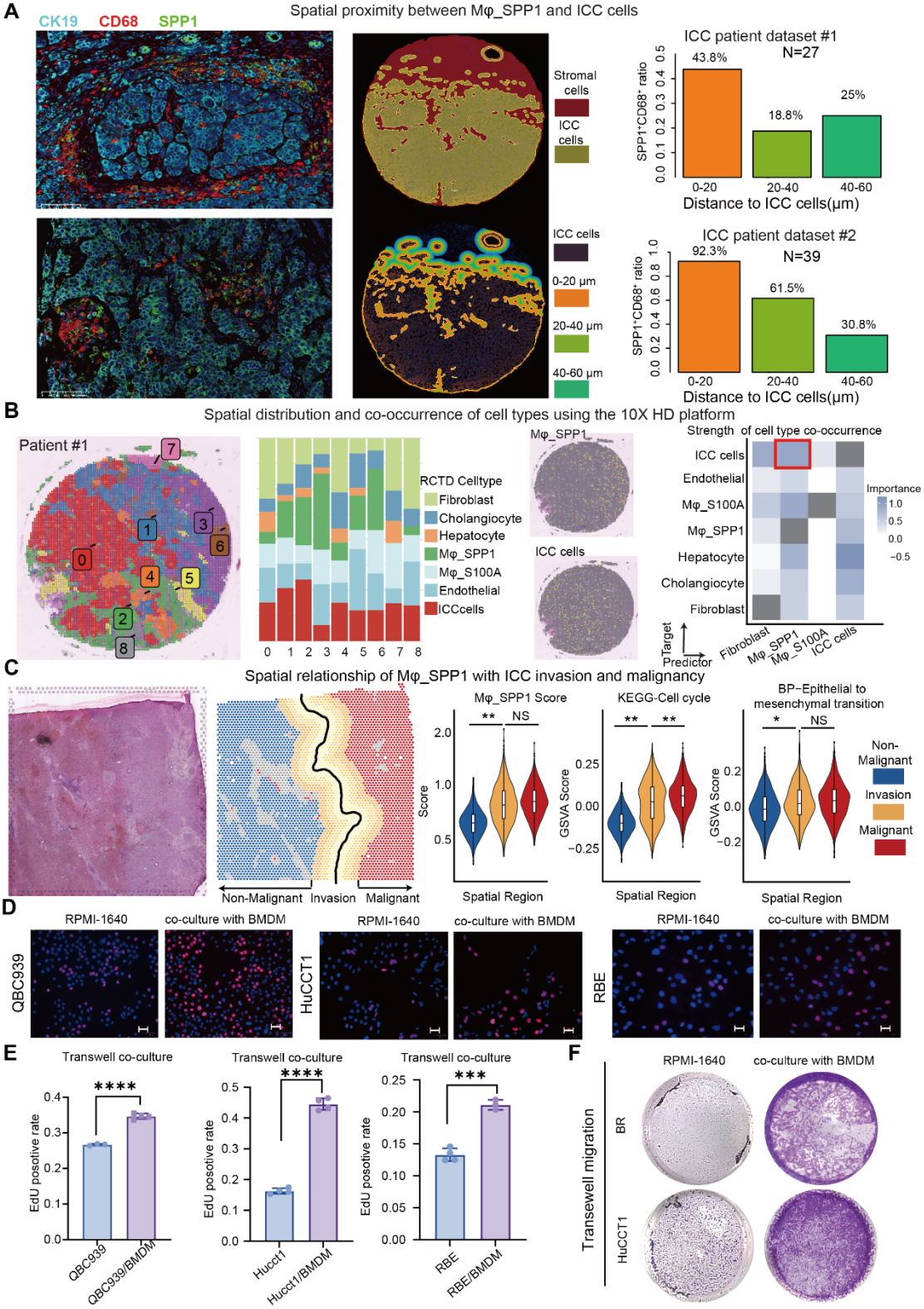
A
CK19
CD68
SPP1
Spatial proximity between Mφ_SPP1 and ICC cells
Stromal cells
ICC cells
ICC patient dataset #1
N=27
43.8%
18.8%
25%
SPP1+CD68+ ratio
0-20
20-40
40-60
Distance to ICC cells(μm)
ICC cells
0-20 μm
20-40 μm
40-60 μm
ICC patient dataset #2
N=39
92.3%
61.5%
30.8%
B
Spatial distribution and co-occurrence of cell types using the 10X HD platform
Patient #1
RCTD Celltype
Fibroblast
Cholangiocyte
Hepatocyte
Mφ_SPP1
Mφ_S100A
Endothelial
ICCcells
Strength of cell type co-occurrence
Importance
Target
Predictor
C
Spatial relationship of Mφ_SPP1 with ICC invasion and malignancy
Non-Malignant
Invasion
Malignant
Mφ_SPP1 Score
KEGG-Cell cycle
BP-Epithelial to mesenchymal transition
Score
GSVA Score
Spatial Region
D
RPMI-1640
co-culture with BMDM
QBC939
HuCCT1
RBE
E
Transwell co-culture
EdU posotive rate
QBC939
QBC939/BMDM
Hucct1
Hucct1/BMDM
RBE/BMDM
F
Transewell migration
BR
HuCCT1

Figure 3

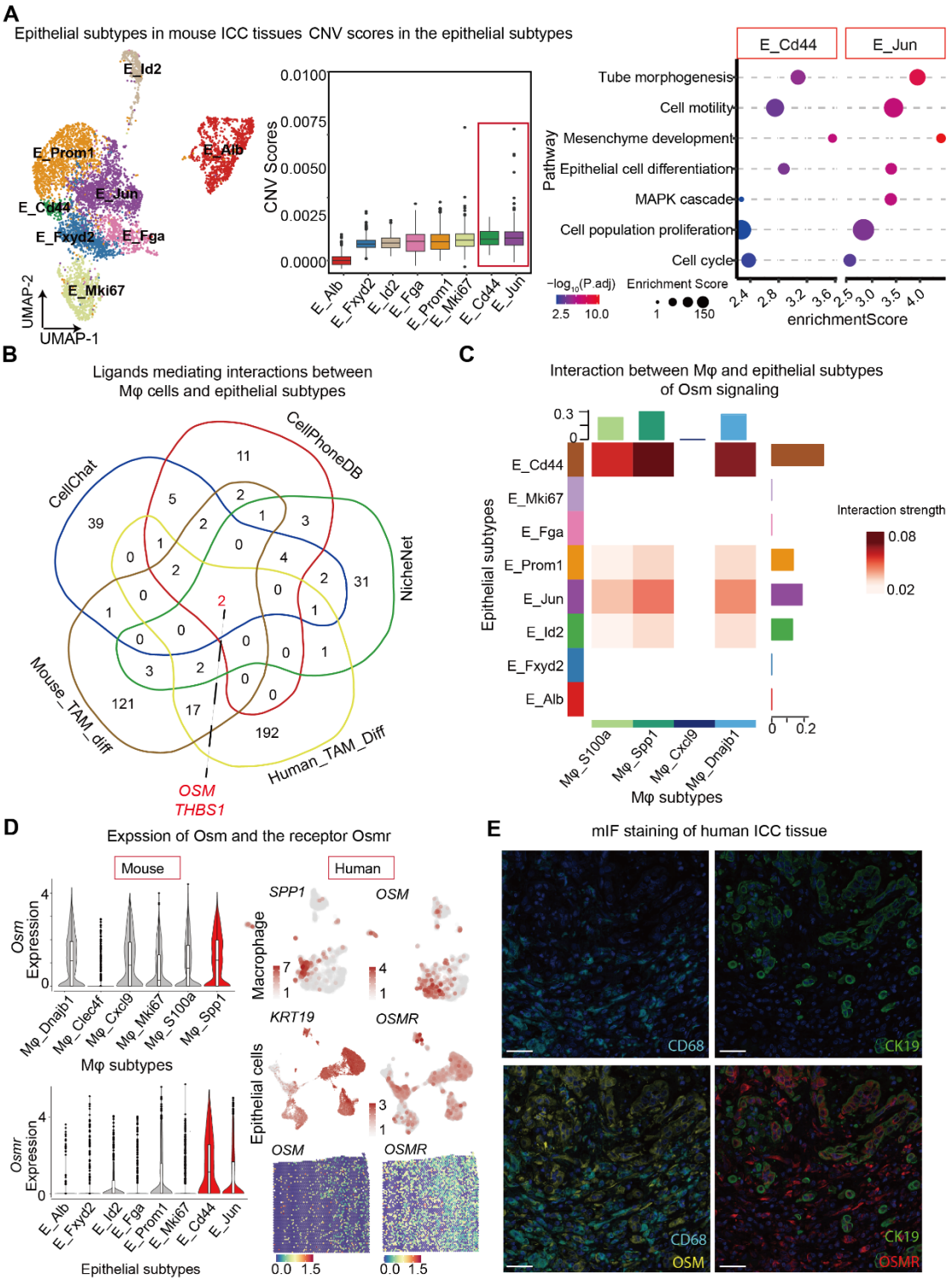
A
Epithelial subtypes in mouse ICC tissues
CNV scores in the epithelial subtypes
E_Id2
E_Prom1
E_Alb
E_Jun
E_Cd44
E_Fxyd2
E_Fga
E_Mki67
UMAP-2
UMAP-1
CNV Scores
0.0100
0.0075
0.0050
0.0025
0.0000
E_Alb
E_Fxyd2
E_Id2
E_Fga
E_Prom1
E_Mki67
E_Cd44
E_Jun
E_Cd44
E_Jun
Pathway
Tube morphogenesis
Cell motility
Mesenchyme development
Epithelial cell differentiation
MAPK cascade
Cell population proliferation
Cell cycle
−log10(P.adj)
2.5
10.0
Enrichment Score
1
150
2.4
2.8
3.2
3.6
2.5
3.0
3.5
4.0
enrichmentScore
B
Ligands mediating interactions between
Mφ cells and epithelial subtypes
CellChat
CellPhoneDB
NicheNet
Mouse_TAM_diff
Human_TAM_Diff
OSM
THBS1
C
Interaction between Mφ and epithelial subtypes
of Osm signaling
Epithelial subtypes
E_Cd44
E_Mki67
E_Fga
E_Prom1
E_Jun
E_Id2
E_Fxyd2
E_Alb
Interaction strength
0.08
0.02
Mφ_S100a
Mφ_Spp1
Mφ_Cxcl9
Mφ_Dnajb1
Mφ subtypes
D
Expssion of Osm and the receptor Osmr
Mouse
Human
Osm
Expression
Mφ_Dnajb1
Mφ_Clec4f
Mφ_Cxcl9
Mφ_Mki67
Mφ_S100a
Mφ_Spp1
Mφ subtypes
SPP1
OSM
Macrophage
KRT19
OSMR
Epithelial cells
Osmr
Expression
E_Alb
E_Fxyd2
E_Id2
E_Fga
E_Prom1
E_Mki67
E_Cd44
E_Jun
Epithelial subtypes
OSM
OSMR
0.0
1.5
E
mIF staining of human ICC tissue
CD68
CK19
CD68
OSM
CK19
OSMR

681

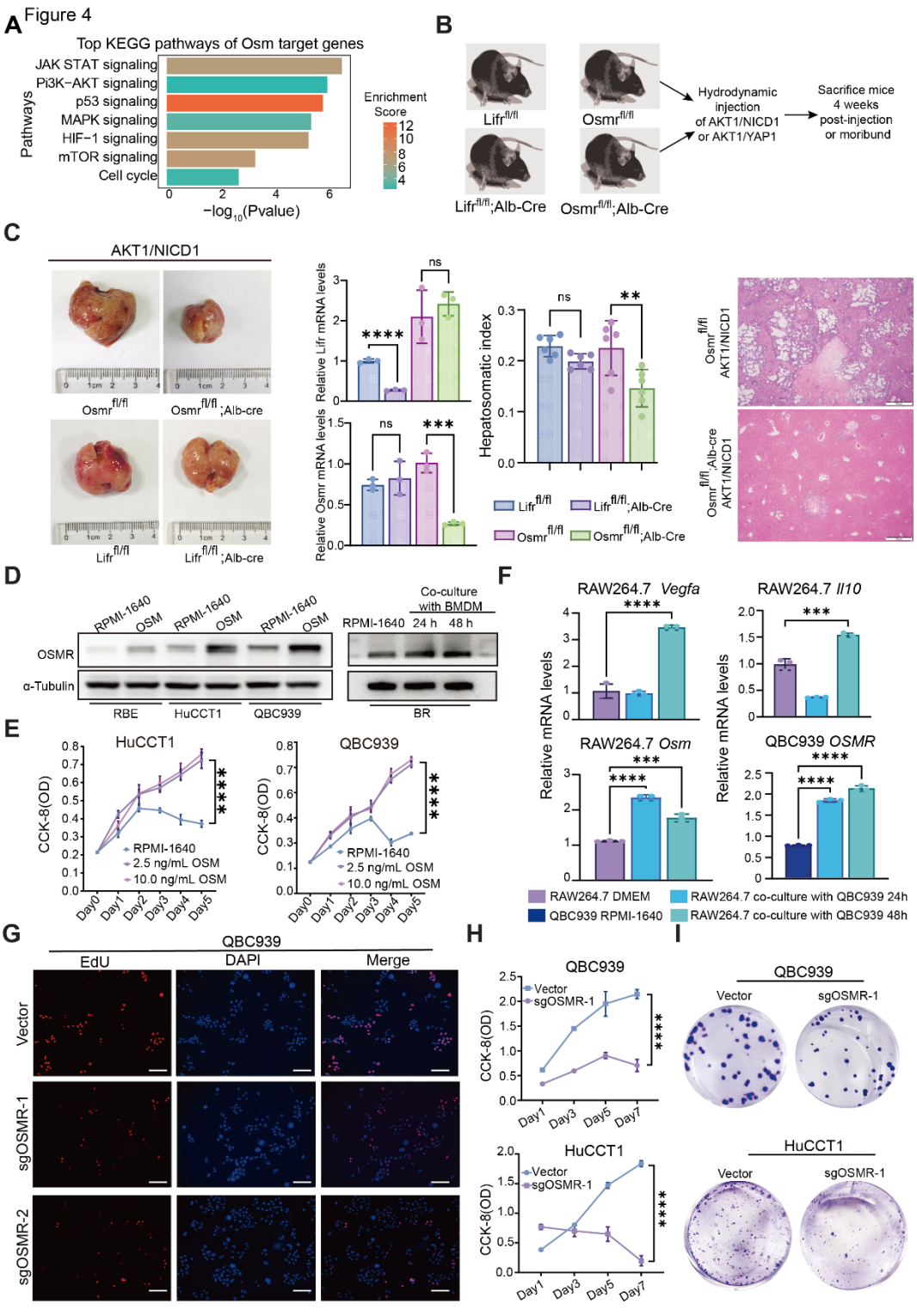
Figure 4
A
Top KEGG pathways of Osm target genes
JAK STAT signaling
Pi3K−AKT signaling
p53 signaling
MAPK signaling
HIF−1 signaling
mTOR signaling
Cell cycle
Pathways
−log10(Pvalue)
Enrichment Score
B
Lifr fl/fl
Osmr fl/fl
Lifr fl/fl;Alb-Cre
Osmr fl/fl;Alb-Cre
Hydrodynamic injection of AKT1/NICD1 or AKT1/YAP1
Sacrifice mice 4 weeks post-injection or moribund
C
AKT1/NICD1
Osmr fl/fl
Osmr fl/fl;Alb-cre
Lifr fl/fl
Lifr fl/fl;Alb-cre
Relative Lifr mRNA levels
Relative Osmr mRNA levels
Hepatosomatic index
Lifr fl/fl
Lifr fl/fl;Alb-Cre
Osmr fl/fl
Osmr fl/fl;Alb-Cre
Osmr fl/fl AKT1/NICD1
Osmr fl/fl;Alb-cre AKT1/NICD1
D
RPMI-1640
OSM
Co-culture with BMDM
24 h
48 h
OSMR
α-Tubulin
RBE
HuCCT1
QBC939
BR
E
HuCCT1
QBC939
CCK-8(OD)
RPMI-1640
2.5 ng/mL OSM
10.0 ng/mL OSM
Day0
Day1
Day2
Day3
Day4
Day5
F
RAW264.7 Vegfa
RAW264.7 Il10
RAW264.7 Osm
QBC939 OSMR
Relative mRNA levels
RAW264.7 DMEM
QBC939 RPMI-1640
RAW264.7 co-culture with QBC939 24h
RAW264.7 co-culture with QBC939 48h
G
QBC939
EdU
DAPI
Merge
Vector
sgOSMR-1
sgOSMR-2
H
QBC939
HuCCT1
Vector
sgOSMR-1
CCK-8(OD)
Day1
Day3
Day5
Day7
I
QBC939
HuCCT1
Vector
sgOSMR-1

682

Figure 5

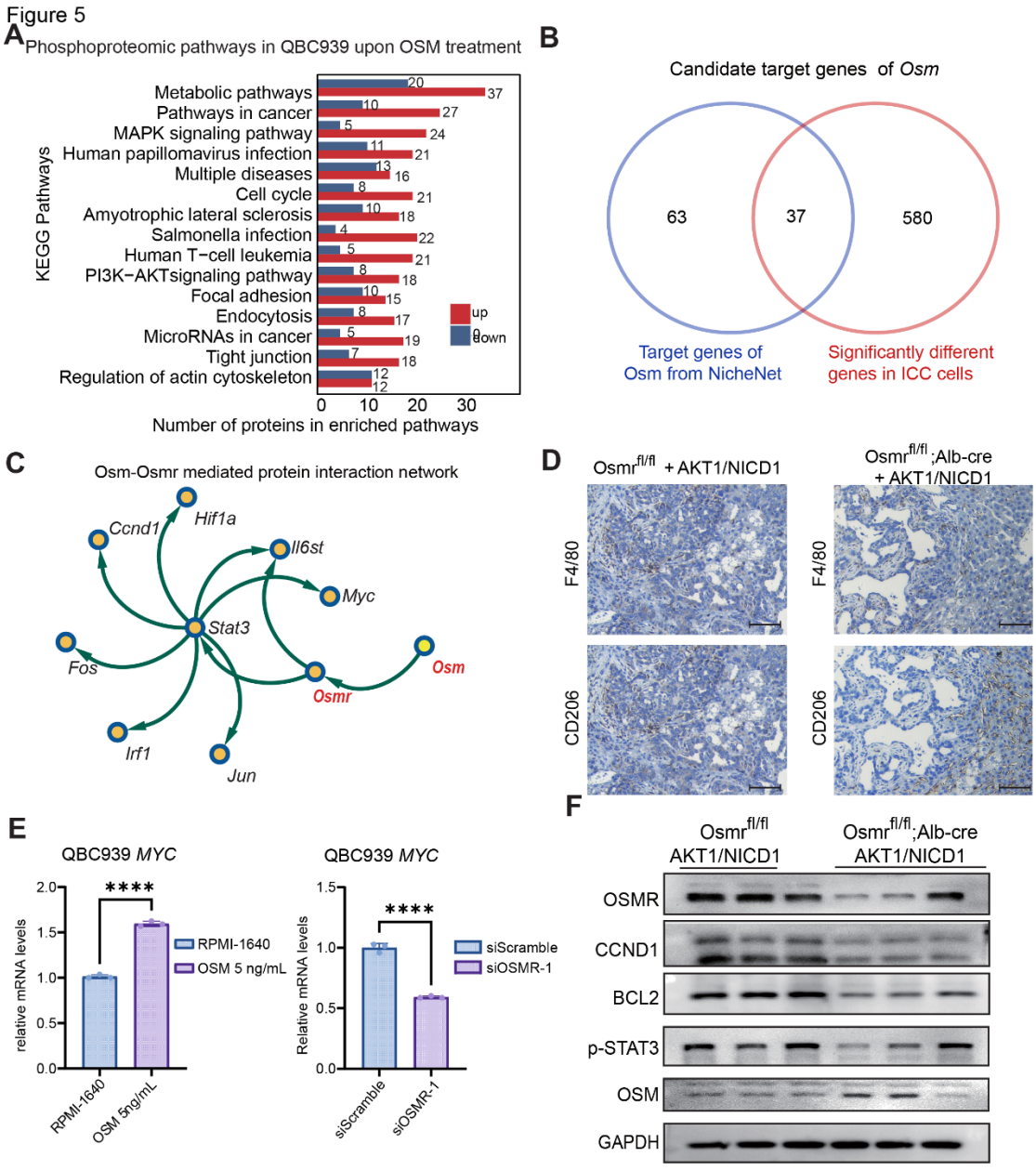
A
Phosphoproteomic pathways in QBC939 upon OSM treatment
KEGG Pathways
Metabolic pathways
Pathways in cancer
MAPK signaling pathway
Human papillomavirus infection
Multiple diseases
Cell cycle
Amyotrophic lateral sclerosis
Salmonella infection
Human T−cell leukemia
PI3K−AKTsignaling pathway
Focal adhesion
Endocytosis
MicroRNAs in cancer
Tight junction
Regulation of actin cytoskeleton
up
down
Number of proteins in enriched pathways
B
Candidate target genes of Osm
63
37
580
Target genes of Osm from NicheNet
Significantly different genes in ICC cells
C
Osm-Osmr mediated protein interaction network
Ccnd1
Hif1a
Il6st
Myc
Stat3
Fos
Osm
Osmr
Irf1
Jun
D
Osmrfl/fl + AKT1/NICD1
Osmrfl/fl;Alb-cre + AKT1/NICD1
F4/80
CD206
E
QBC939 MYC
relative mRNA levels
RPMI-1640
OSM 5 ng/mL
****
QBC939 MYC
Relative mRNA levels
siScramble
siOSMR-1
****
F
Osmrfl/fl AKT1/NICD1
Osmrfl/fl;Alb-cre AKT1/NICD1
OSMR
CCND1
BCL2
p-STAT3
OSM
GAPDH

683

Figure 6

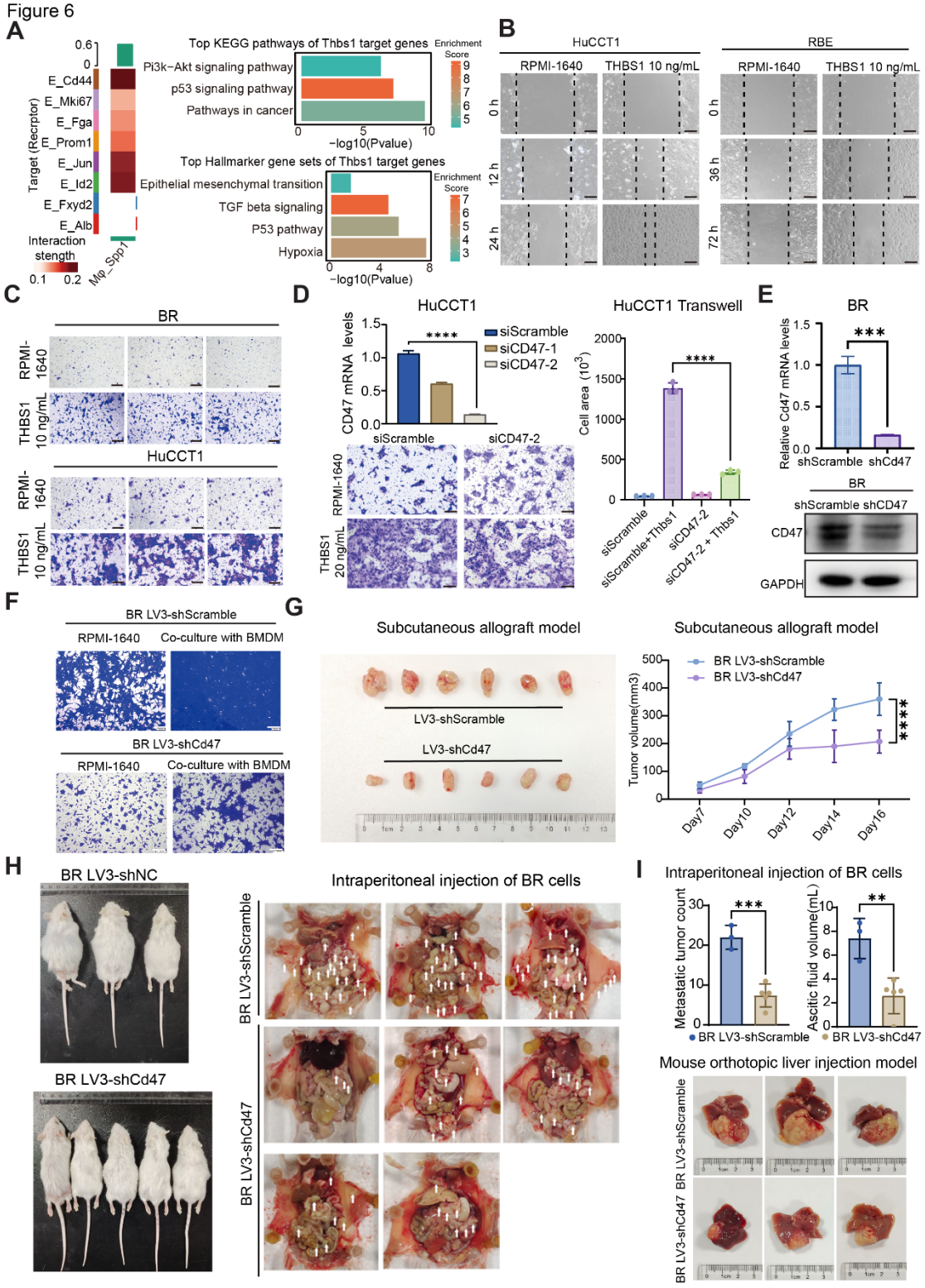
A
Top KEGG pathways of Thbs1 target genes
Pi3k−Akt signaling pathway
p53 signaling pathway
Pathways in cancer
−log10(Pvalue)
Enrichment Score
Top Hallmarker gene sets of Thbs1 target genes
Epithelial mesenchymal transition
TGF beta signaling
P53 pathway
Hypoxia
Target (Recrptor)
E_Cd44
E_Mki67
E_Fga
E_Prom1
E_Jun
E_Id2
E_Fxyd2
E_Alb
Interaction stength
Mφ_Spp1
B
HuCCT1
RBE
RPMI-1640
THBS1 10 ng/mL
0 h
12 h
24 h
36 h
72 h
C
BR
HuCCT1
RPMI-1640
THBS1 10 ng/mL
D
HuCCT1
CD47 mRNA levels
siScramble
siCD47-1
siCD47-2
RPMI-1640
THBS1 20 ng/mL
HuCCT1 Transwell
Cell area (10^3)
siScramble
siScramble+Thbs1
siCD47-2
siCD47-2 + Thbs1
E
BR
Relative Cd47 mRNA levels
shScramble
shCd47
CD47
GAPDH
F
BR LV3-shScramble
RPMI-1640
Co-culture with BMDM
BR LV3-shCd47
G
Subcutaneous allograft model
LV3-shScramble
LV3-shCd47
Tumor volume(mm3)
Day7
Day10
Day12
Day14
Day16
H
BR LV3-shNC
BR LV3-shCd47
Intraperitoneal injection of BR cells
I
Metastatic tumor count
Ascitic fluid volume(mL)
Mouse orthotopic liver injection model

684

Figure 7

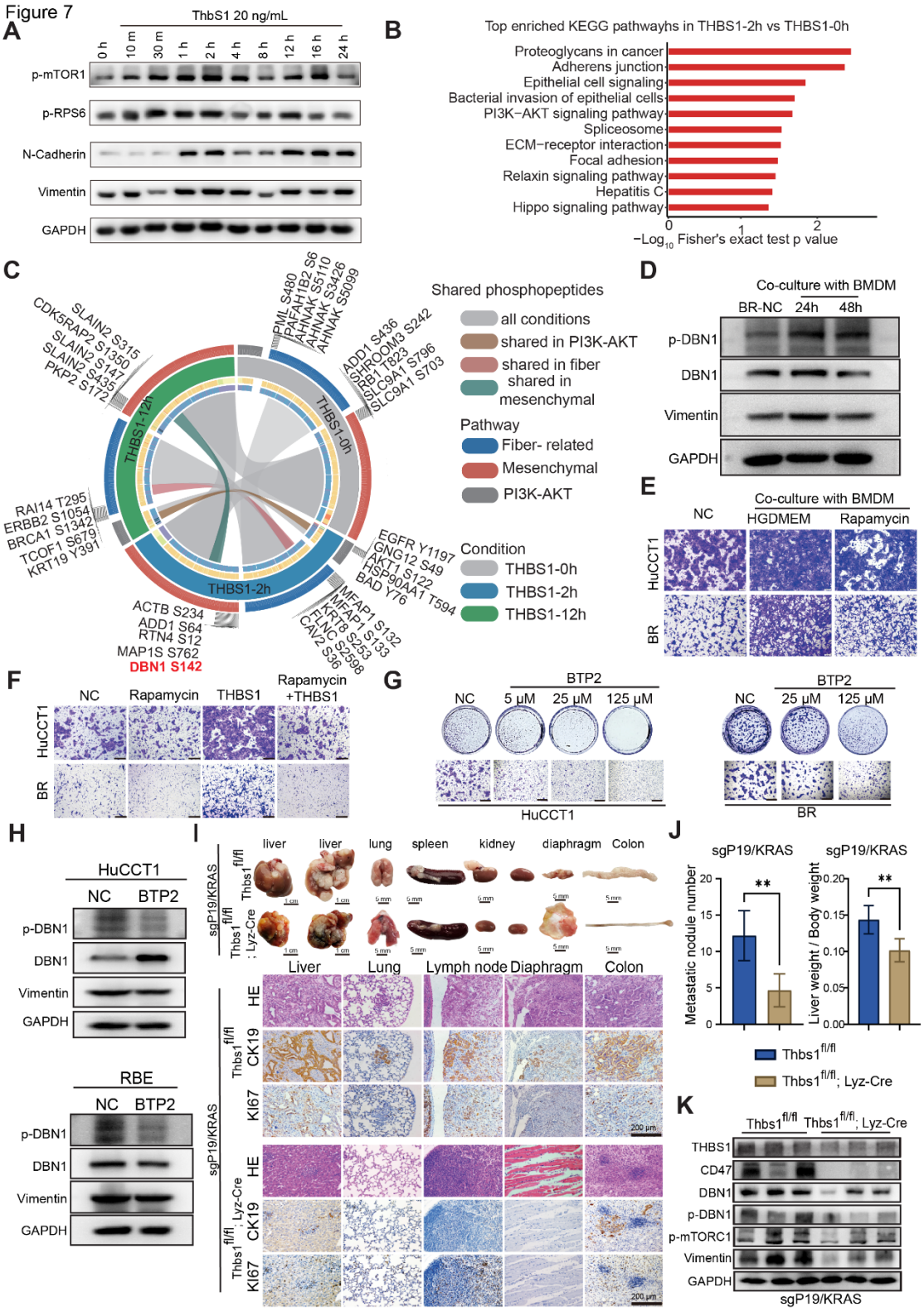
A
ThbS1 20 ng/mL
0 h
10 m
30 m
1 h
2 h
4 h
8 h
12 h
16 h
24 h
p-mTOR1
p-RPS6
N-Cadherin
Vimentin
GAPDH
B
Top enriched KEGG pathwayhs in THBS1-2h vs THBS1-0h
Proteoglycans in cancer
Adherens junction
Epithelial cell signaling
Bacterial invasion of epithelial cells
PI3K−AKT signaling pathway
Spliceosome
ECM−receptor interaction
Focal adhesion
Relaxin signaling pathway
Hepatitis C
Hippo signaling pathway
−Log10 Fisher's exact test p value
C
Shared phosphopeptides
all conditions
shared in PI3K-AKT
shared in fiber
shared in mesenchymal
Pathway
Fiber- related
Mesenchymal
PI3K-AKT
Condition
THBS1-0h
THBS1-2h
THBS1-12h
THBS1-0h
THBS1-2h
THBS1-12h
DBN1 S142
D
Co-culture with BMDM
BR-NC
24h
48h
p-DBN1
DBN1
Vimentin
GAPDH
E
Co-culture with BMDM
NC
HGDMEM
Rapamycin
HuCCT1
BR
F
NC
Rapamycin
THBS1
Rapamycin +THBS1
HuCCT1
BR
G
BTP2
NC
5 μM
25 μM
125 μM
HuCCT1
BR
H
HuCCT1
NC
BTP2
p-DBN1
DBN1
Vimentin
GAPDH
RBE
NC
BTP2
p-DBN1
DBN1
Vimentin
GAPDH
I
sgP19/KRAS
Thbs1fl/fl
Thbs1fl/fl; Lyz-Cre
liver
lung
spleen
kidney
diaphragm
Colon
Liver
Lung
Lymph node
Diaphragm
Colon
HE
CK19
KI67
200 μm
J
sgP19/KRAS
Metastatic nodule number
Liver weight / Body weight
**
Thbs1fl/fl
Thbs1fl/fl; Lyz-Cre
K
Thbs1fl/fl
Thbs1fl/fl; Lyz-Cre
THBS1
CD47
DBN1
p-DBN1
p-mTORC1
Vimentin
GAPDH
sgP19/KRAS

685

Figure 8

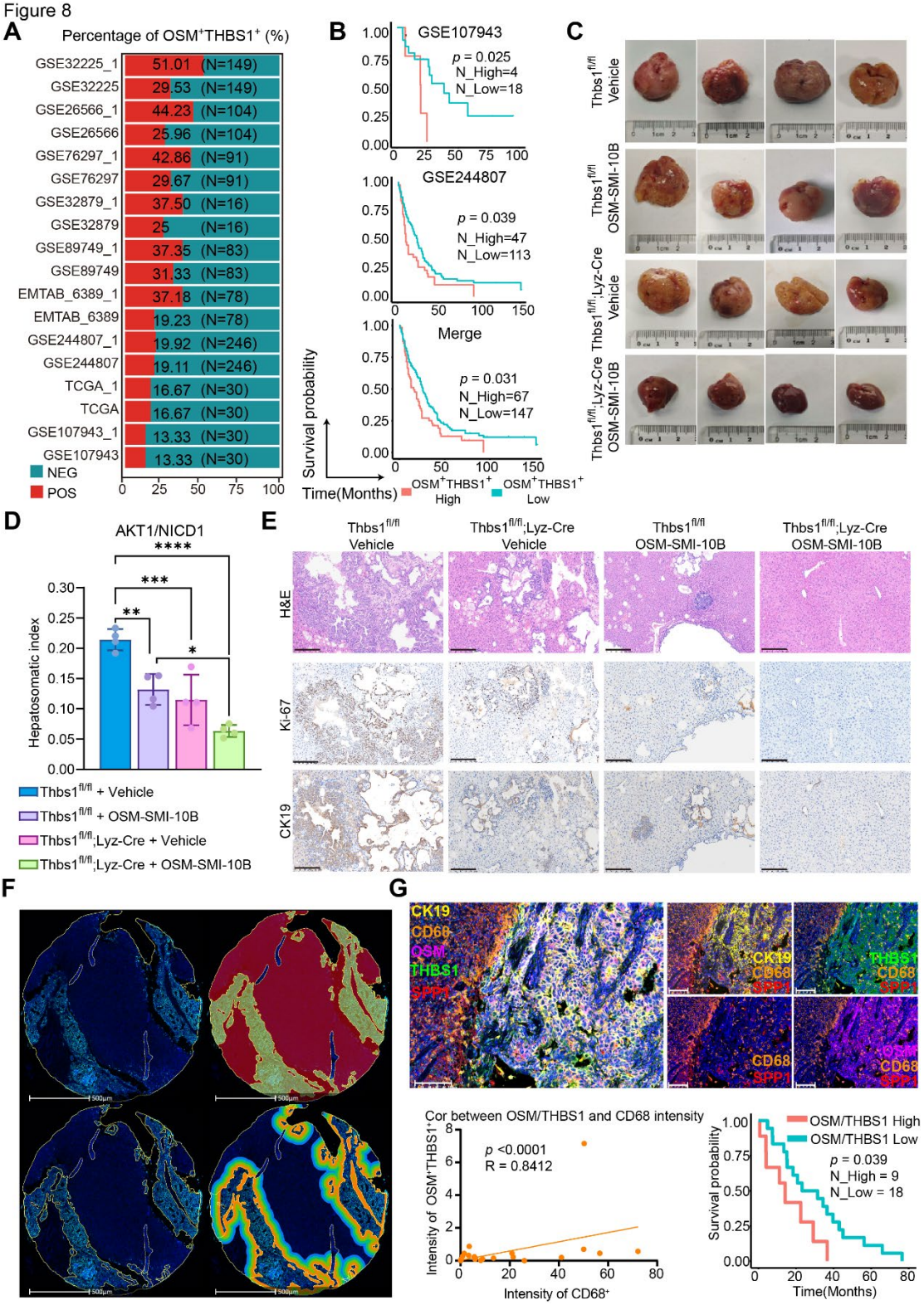
A
Percentage of OSM+THBS1+ (%)
GSE32225_1 51.01 (N=149)
GSE32225 29.53 (N=149)
GSE26566_1 44.23 (N=104)
GSE26566 25.96 (N=104)
GSE76297_1 42.86 (N=91)
GSE76297 29.67 (N=91)
GSE32879_1 37.50 (N=16)
GSE32879 25 (N=16)
GSE89749_1 37.35 (N=83)
GSE89749 31.33 (N=83)
EMTAB_6389_1 37.18 (N=78)
EMTAB_6389 19.23 (N=78)
GSE244807_1 19.92 (N=246)
GSE244807 19.11 (N=246)
TCGA_1 16.67 (N=30)
TCGA 16.67 (N=30)
GSE107943_1 13.33 (N=30)
GSE107943 13.33 (N=30)
NEG
POS
B
GSE107943
p = 0.025
N_High=4
N_Low=18
GSE244807
p = 0.039
N_High=47
N_Low=113
Merge
p = 0.031
N_High=67
N_Low=147
Survival probability
Time(Months)
OSM+THBS1+ High
OSM+THBS1+ Low
C
Thbs1fl/fl Vehicle
Thbs1fl/fl OSM-SMI-10B
Thbs1fl/fl;Lyz-Cre Vehicle
Thbs1fl/fl;Lyz-Cre OSM-SMI-10B
D
AKT1/NICD1
Hepatosomatic index
Thbs1fl/fl + Vehicle
Thbs1fl/fl + OSM-SMI-10B
Thbs1fl/fl;Lyz-Cre + Vehicle
Thbs1fl/fl;Lyz-Cre + OSM-SMI-10B
E
Thbs1fl/fl Vehicle
Thbs1fl/fl;Lyz-Cre Vehicle
Thbs1fl/fl OSM-SMI-10B
Thbs1fl/fl;Lyz-Cre OSM-SMI-10B
H&E
Ki-67
CK19
F
G
CK19
CD68
OSM
THBS1
SPP1
Cor between OSM/THBS1 and CD68 intensity
p <0.0001
R = 0.8412
Intensity of OSM+THBS1+
Intensity of CD68+
OSM/THBS1 High
OSM/THBS1 Low
p = 0.039
N_High = 9
N_Low = 18
Survival probability
Time(Months)

686